Research Square

Preprints are preliminary reports that have not undergone peer review.
They should not be considered conclusive, used to inform clinical practice,
or referenced by the media as validated information.

Longitudinal OCT/OCTA Imaging Reveals Early Neurovascular Dysfunction Associated with Ferroptosis-Related Metabolic Stress in Experimental Diabetic Retinopathy

CHUAN PENG
Shanghai Institute of Technology
XIANGNING WANG
Shanghai Sixth People's Hospital, Shanghai Jiao Tong University School of Medicine
JIABIAO LIU
Shanghai Sixth People's Hospital, Shanghai Jiao Tong University School of Medicine
MINGJIE NI
Shanghai Institute of Technology
WENJUAN WU
Shanghai Institute of Technology
SHENGXI MENG
Shanghai Sixth People's Hospital, Shanghai Jiao Tong University School of Medicine
CUIXIA DAI
sdadai7412@163.com

Shanghai Institute of Technology

Research Article

Keywords: Diabetic retinopathy, Ferroptosis, OCT, OCTA, Multimodal imaging

Posted Date: November 5th, 2026

DOI: https://doi.org/10.21203/rs.3.rs-11335854/v1

License: This work is licensed under a Creative Commons Attribution 4.0 International License.
Read Full License

Additional Declarations: No competing interests reported.

Abstract

Diabetic retinopathy (DR) involves early neurovascular and metabolic dysfunction. We evaluated whether longitudinal optical coherence tomography (OCT) and OCT angiography (OCTA) can provide in vivo phenotypic readouts of ferroptosis-related retinal injury in streptozotocin-induced diabetic rats. Diabetes caused progressive retinal thinning, reduced capillary plexus vessel area density, and impaired photopic negative responses, accompanied by iron accumulation, lipid peroxidation, reduced antioxidant capacity, and altered ferroptosis-associated protein expression. Liproxstatin-1 partially attenuated these abnormalities. Exploratory analyses further linked OCTA and electrophysiological phenotypes with ferroptosis-related measures. These findings support OCT/OCTA as noninvasive longitudinal readouts of early diabetic retinal injury associated with ferroptosis-related metabolic stress.

1. Introduction

Diabetic retinopathy (DR) is a leading cause of vision impairment worldwide and has traditionally been characterized as a microvascular complication of diabetes mellitus [1]. Increasing evidence, however, indicates that diabetic retinal injury is a neurovascular process in which neuronal dysfunction, glial alterations, metabolic stress. This broader view creates a need for quantitative in vivo readouts that can track early structural, vascular, and functional changes longitudinally rather than relying exclusively on end-stage histopathology.

Among the emerging mechanisms implicated in diabetic retinal injury, ferroptosis-associated metabolic dysregulation has attracted increasing attention. It is an iron-dependent form of regulated cell death characterized by iron accumulation, lipid peroxidation, and failure of antioxidant defense systems [2]. Hyperglycemia can disturb iron homeostasis, mitochondrial function, glutathione metabolism, and reactive oxygen species balance, thereby increasing retinal susceptibility to ferroptosis-related injury [3, 4]. Because neurons, glia, and vascular endothelial cells are functionally coupled within the retinal neurovascular unit, ferroptosis-associated stress could plausibly produce coordinated structural, microvascular, and functional abnormalities.

Experimental evidence supports the involvement of ferroptosis-related pathways in diabetic retinal damage, including microvascular dysfunction, mitochondrial injury, neuronal impairment, lipid peroxidation, and altered GPX4/System Xc-signaling [5–8]. Pharmacologic inhibition of ferroptosis-associated processes has also shown protective effects in preclinical models. Nevertheless, most of this evidence is derived from molecular assays, cell culture, histology, or terminal tissue analysis, which limits direct assessment of how these molecular alterations evolve together with measurable retinal phenotypes in vivo [9, 10].

OCT provides depth-resolved, noninvasive visualization of retinal microstructure, whereas OCTA extends OCT by using motion contrast to map retinal microvascular flow without exogenous dye [11, 12]. Their ability to repeatedly quantify layer-specific structure and vascular flow signals makes OCT/OCTA well suited to longitudinal studies of early diabetic retinal injury. However, OCT/OCTA parameters are

phenotypic rather than molecularly specific: retinal thinning or reduced OCTA flow signal can arise from multiple pathophysiological processes. A central question is therefore whether optical imaging phenotypes co-vary with ferroptosis-associated metabolic alterations strongly enough to provide useful in vivo readouts of disease evolution.

To address this question, we established a longitudinal imaging-to-molecular framework in a streptozotocin (STZ)-induced diabetic rat model. Spectral-domain OCT was used to quantify full-retinal and layer-specific thickness, OCTA was used to quantify superficial and deep capillary plexus vessel area density, and electroretinography (ERG) with PhNR analysis was used as a complementary functional assessment. Imaging and electrophysiological measurements were integrated with histology, ferroptosis-associated protein expression, Fe^{2+} accumulation, lipid peroxidation, antioxidant capacity, and pharmacological intervention with Liproxstatin-1.

We hypothesized that early experimental diabetes would produce coordinated structural, microvascular, functional, and ferroptosis-associated metabolic abnormalities, and that selected OCT/OCTA and ERG parameters would show measurable associations with the molecular phenotype. By integrating longitudinal multimodal retinal imaging with molecular analyses and pharmacological intervention, this study aimed to establish an experimental imaging-to-molecular framework linking ferroptosis-associated metabolic stress with measurable retinal neurovascular alterations during early diabetic retinal disease.

2. Materials and Methods

2.1 Experimental animals

Male Sprague-Dawley rats aged 6–7 weeks and weighing approximately 220 g were obtained from Shanghai Jiesijie Laboratory Animal Co., Ltd. (Shanghai, China). Animals were housed at 22 ± 2°C and 60% ± 5% relative humidity under a 12-h light/12-h dark cycle with free access to standard chow and water. Only male rats were included to reduce biological variability related to sex-dependent regulation of iron metabolism and oxidative stress.

Diabetes was induced with a single intraperitoneal STZ injection (65 mg/kg; Macklin) in 20 mM citrate buffer (pH 4.5); controls received buffer. Fasting blood glucose and weight were monitored weekly. Diabetes was confirmed by fasting glucose ≥ 16.7 mmol/L on two consecutive measurements.

Rats were assigned to normal control (NC), diabetes (DM), and liproxstatin-1-treated diabetes (DM + Lx-1) groups (n = 5 each). Liproxstatin-1 (10 mg/kg; MedChemExpress) was injected intraperitoneally every other day during weeks 6–8.

For imaging, rats received intraperitoneal pentobarbital (40 mg/kg), 1% tropicamide, and topical 0.5% proparacaine; corneal hydration and body temperature were maintained.

Procedures were approved by the Ethics Committee of Shanghai Institute of Technology and followed the Guide for the Care and Use of Laboratory Animals.

2.2 Ophthalmic multimodal imaging system

A small-animal ophthalmic multimodal imaging system (Haojing® Saris, Nanjing Boshi Medical Technology Co., Ltd., Nanjing, China) was used for retinal imaging. Spectral-domain OCT (SD-OCT) provided cross-sectional structural imaging, and OCTA provided depth-resolved retinal microvascular flow contrast.

The OCT system was equipped with a broadband light source centered at 850 nm with a bandwidth of 100 nm and operated at an A-scan rate of 100,000 A-scans/s. The theoretical transverse and axial resolutions were 3.3 μm and 3.9 μm in air, respectively, with an imaging depth of 3.7 mm. For structural imaging, each OCT volume consisted of 512 A-scans × 512 B-scans and covered a 50° field of view. Three repeated B-scans were acquired at each retinal location and averaged to reduce speckle noise. Retinal boundaries were automatically segmented by the imaging software and manually corrected when necessary.

For OCTA imaging, retinal microvascular flow maps were generated using the optical microangiography (OMAG) algorithm. Three repeated OCTA scans were acquired at each retinal location, registered, and averaged to reduce speckle noise and improve vascular continuity. OCTA images were automatically segmented into the superficial capillary plexus (SCP) and deep capillary plexus (DCP) according to the retinal layer boundaries defined by the imaging system. Segmentation boundaries were manually inspected and corrected when necessary. En face OCTA maximum-intensity-projection images were generated for each vascular plexus. To minimize potential projection artifacts and segmentation errors, OCTA images were carefully reviewed for vascular duplication, mis-segmentation, and motion artifacts before quantitative analysis.

For quantitative analysis, a standardized annular region of interest (ROI) centered on the optic nerve head was used, with an inner diameter of 350 μm and an outer diameter of 500 μm. The same ROI configuration was applied across all animals and imaging time points. The peripapillary region was selected because rats lack a macula and this region provides consistent anatomical landmarks for longitudinal analysis. The annular ROI was selected to improve measurement reproducibility, reduce edge-related artifacts, and facilitate longitudinal comparison [13, 14].

2.3 Photopic negative response (PhNR) recording

Electroretinography was recorded with the Celeris system and Espion V6 software (Diagnosys). Following overnight dark adaptation, a-wave, b-wave, and PhNR amplitudes were assessed; PhNR amplitude was defined relative to baseline at its trough [15, 16]

2.4 Hematoxylin and eosin (H&E) staining

At the study endpoint, left eyes were enucleated for histological analysis. Eyeballs were fixed, paraffin-embedded, and sectioned at 5 μm thickness. Sections were deparaffinized, rehydrated, stained with hematoxylin and eosin, and imaged using a light microscope (SWE-CX63, Servicebio, China). Retinal structural organization and layer morphology were evaluated qualitatively.

2.5 Western blot analysis of retinal protein expression

Right retinas were frozen at -80°C and lysed in RIPA/PMSF (Beyotime). Proteins (30 μg/lane) underwent 10% SDS-PAGE and PVDF transfer. Membranes were blocked in 5% BSA/TBST, incubated with TFRC (ET1702-65), ACSL4 (ET1702-37), SLC7A11, GPX4 (ET1603-24), and β-actin antibodies (all 1:1000; HUABIO), followed by HRP-conjugated secondary antibodies (1:1000). Chemiluminescent bands were quantified using ImageJ and normalized to β-actin.

2.6 Biochemical Assays

Retinal iron accumulation, antioxidant capacity, and lipid peroxidation were assessed in tissue homogenates using commercial assays according to the manufacturers' instructions. Technical duplicate measurements were averaged before statistical analysis. Total superoxide dismutase (SOD) activity was measured using a WST-8-based kit (S0101S; Beyotime). Malondialdehyde (MDA), used as an index of lipid peroxidation, was measured using kit S0131S (Beyotime). Retinal Fe^{2+} concentration was quantified using a micro-method iron assay kit (D799346; Sangon Biotech).

2.7 Statistical analysis

Statistical analyses were performed in GraphPad Prism 9 (GraphPad Software, Boston, MA, USA). The individual animal was treated as the independent experimental unit; technical replicates were averaged before statistical testing. Data are presented as mean ± standard deviation (SD) unless otherwise stated.

Longitudinal outcomes were analyzed using two-way mixed-effects models with group, time, and repeated animal measurements, followed where appropriate by Tukey-adjusted comparisons. Endpoint outcomes were evaluated using one-way ANOVA and Tukey tests after checking assumptions.

Selected pooled associations were assessed with Pearson correlations and linear regression. Cohen’s d and 95% confidence intervals were estimated for selected pairwise comparisons. Given the small sample and pooling of treatment groups, associations were exploratory, not causal. All tests were two-sided ($p < 0.05$).

3. Results

3.1 Changes in body weight and blood glucose levels

Following STZ administration, diabetic rats developed persistent hyperglycemia and impaired weight gain compared with control animals (Fig. 1). Control animals showed progressive increases in body weight, whereas diabetic animals exhibited minimal weight gain. FBG remained markedly elevated

throughout follow-up, reaching approximately 30 mmol/L in diabetic animals ($p < 0.0001$ vs NC). Liproxstatin-1 did not normalize blood glucose levels but was accompanied by a partial improvement in body-weight trajectory relative to untreated diabetic animals.

3.2 Progressive retinal structural alterations detected by OCT

Longitudinal OCT imaging was performed over five weeks beginning at week 3 after diabetes induction to characterize the temporal evolution of retinal structural alterations and to evaluate the effects of Liproxstatin-1 treatment. Representative OCT images and quantitative analyses are shown in Fig. 2. Retinal thickness measurements were initiated at week 3 because overt structural alterations were not evident during the initial induction phase.

Compared with the NC group, diabetic animals exhibited progressive reductions in total retinal thickness during the observation period. Full retinal thickness, measured from the internal limiting membrane to the retinal pigment epithelium, decreased from 225.23 ± 8.56 μm to 203.00 ± 10.35 μm in the DM group ($p < 0.0001$). Layer-specific analysis demonstrated significant reductions in the thickness of the ganglion cell complex (GCC), inner nuclear layer (INL), and outer nuclear layer (ONL), with changes of − 8.36 ± 2.18 μm ($p < 0.0001$), − 5.41 ± 2.11 μm ($p < 0.0001$), and − 8.86 ± 1.20 μm ($p < 0.0001$), respectively.

In diabetic animals treated with Liproxstatin-1, retinal thinning was partially attenuated. Compared with untreated diabetic animals, GCC, INL, and ONL thicknesses were greater by 4.31 ± 0.20 μm, 5.29 ± 2.01 μm, and 6.68 ± 1.12 μm, respectively.

3.3 Alterations in superficial and deep capillary plexus vessel density

Longitudinal OCTA analysis was performed to assess retinal microvascular alterations during diabetes progression and after Lx-1 intervention. Representative en face OCTA images are shown in Fig. 3A-B.

Compared with the NC group, diabetic animals exhibited progressive reductions in vessel area density in both the superficial capillary plexus (SCP) and deep capillary plexus (DCP), accompanied by focal areas of capillary rarefaction. Quantitative analysis showed that SCP vessel area density decreased from 46.4% ± 2.3% to 42.2% ± 1.9%, whereas DCP vessel area density decreased from 47.5% ± 1.8% to 42.7% ± 1.6% during the observation period (Fig. 3C–D).

Following Liproxstatin-1 treatment, partial recovery of vessel area density was observed in both vascular plexuses. SCP and DCP vessel area densities increased to 44.6% ± 1.9% and 46.1% ± 2.4%, respectively, compared with untreated diabetic animals.

The magnitude of reduction appeared numerically greater in the DCP than in the SCP during the observation period.

3.4 Effects of ferroptosis inhibition on retinal neurofunctional status

ERG recordings showed impaired retinal electrophysiological responses in diabetic animals (Fig. 4). The most prominent changes were observed in the b-wave and PhNR. Mean b-wave amplitude decreased from 51.42 ± 10.3 μV in NC animals to 24.35 ± 5.4 μV in DM animals ($p < 0.001$), and PhNR amplitude decreased from 49.5 ± 6.6 μV to 23.7 ± 5.3 μV ($p < 0.001$). The a-wave showed a smaller change.

Following Liproxstatin-1 treatment, b-wave amplitude increased to 35.87 ± 5.8 μV and PhNR amplitude to 36.5 ± 4.7 μV relative to untreated diabetic animals, indicating partial functional preservation.

3.5 Ferroptosis-associated metabolic alterations in diabetic retina

To characterize ferroptosis-associated molecular and oxidative alterations in diabetic retinal tissue, retinal histology, protein expression, iron accumulation, lipid peroxidation, and antioxidant capacity were evaluated at the experimental endpoint (Fig. 5).

H&E staining revealed retinal thinning and alterations in cellular organization within the inner and outer nuclear layers in diabetic animals. These histological findings were consistent with the structural changes observed by OCT.

Western blot analysis revealed altered expression of ferroptosis-associated regulatory proteins in diabetic retinas. Specifically, diabetic conditions were associated with reduced expression of antioxidant regulators, including GPX4 and SLC7A11, accompanied by increased expression of proteins involved in iron metabolism and lipid oxidation regulation, including TFRC and ACSL4 (Fig. 5B-C).

Diabetic retinas demonstrated increased Fe^{2+} accumulation compared with control tissues ($P < 0.001$). In parallel, lipid peroxidation levels were elevated, as indicated by increased MDA concentrations, whereas antioxidant capacity was reduced, reflected by decreased SOD activity (Fig. 5D-F).

Collectively, these findings demonstrate coordinated alterations in ferroptosis-associated molecular markers, iron accumulation, lipid peroxidation, and antioxidant capacity in diabetic retinal tissue. The partial normalization of these parameters following Liproxstatin-1 treatment provides pharmacological support for the involvement of ferroptosis-associated metabolic stress in experimental diabetic retinal injury.

3.6 Exploratory associations between retinal neurovascular alterations and ferroptosis-associated molecular markers

Exploratory analyses were performed to assess whether selected in vivo retinal phenotypes tracked with ferroptosis-associated biochemical measures.

DCP VAD showed a large NC-versus-DM effect size (Cohen's d = 4.12, 95% CI: 1.80–6.44). In pooled analyses across the three groups (n = 15), DCP VAD was inversely associated with retinal Fe^{2+} concentration ($r = -0.82$, $p < 0.001$) and MDA ($r = -0.80$, $p < 0.001$), and positively associated with GPX4 expression ($r = 0.75$, $p < 0.01$) (Fig. 6A-C).

PhNR amplitude also showed a large NC-versus-DM effect size (Cohen's d = 3.87, 95% CI: 1.63–6.10). In pooled analyses, PhNR amplitude was inversely associated with Fe^{2+} concentration ($r = -0.73$, $p < 0.01$) and MDA ($r = -0.83$, $p < 0.001$) (Fig. 6D,E).

These pooled correlations are strongly influenced by the separation among experimental groups and therefore should not be interpreted as within-group mechanistic relationships or evidence of causality. They are presented as exploratory imaging-to-molecular associations that require validation in larger, independent cohorts.

Overall, the combined longitudinal and endpoint data show that OCTA-derived vascular changes and PhNR dysfunction co-vary with ferroptosis-associated metabolic abnormalities during early experimental diabetic retinal injury.

4. Discussion

In this study, multimodal retinal imaging was integrated with biochemical analyses to investigate whether ferroptosis-associated metabolic stress is accompanied by early neurovascular dysfunction in diabetic retinopathy. By combining OCT, OCTA, and ERG with molecular assays, coordinated structural, vascular, functional, and metabolic alterations were identified in an STZ-induced diabetic rat model.

One of the major observations of this study was that the numerical reduction was greater in the DCP. This finding suggests that the deep retinal microvasculature may represent a particularly vulnerable compartment during early diabetic retinal injury. The DCP supplies oxygen and nutrients to metabolically active inner retinal neurons and has been reported to be especially susceptible to hypoxia, oxidative stress, and mitochondrial dysfunction under diabetic conditions [17, 18]. Hyperglycemia-induced oxidative and ferroptosis-associated lipid peroxidation may contribute to endothelial and neurovascular dysfunction within the DCP. In parallel, PhNR reduction indicates early retinal ganglion cell dysfunction, which is also highly sensitive to redox imbalance [19, 20]. The coordinated alterations observed in DCP density and PhNR further support the presence of coupled neurovascular vulnerability under ferroptosis-associated metabolic stress.

The observed imaging and functional alterations may reflect downstream consequences of ferroptosis-associated lipid peroxidation and membrane injury within the retinal neurovascular unit. Excessive oxidative damage in neuronal and endothelial membranes could contribute to retinal thinning, capillary rarefaction, and impaired electrophysiological responses detectable by OCT/OCTA and ERG. Within this framework, ferroptosis-associated metabolic dysregulation may serve as a mechanistic link connecting hyperglycemia-induced oxidative stress with early neurovascular dysfunction in diabetic retina.

Furthermore, treatment with Liproxstatin-1 partially ameliorated both molecular abnormalities and corresponding imaging and functional alterations, providing additional support for the involvement of ferroptosis-related pathways in diabetic retinal neurovascular injury. Although Liproxstatin-1 may exert pleiotropic antioxidant effects beyond ferroptosis inhibition [21, 22], the concurrent improvement observed across molecular, vascular, structural, and electrophysiological parameters supports the pathological relevance of ferroptosis-associated metabolic stress in early DR.

From a translational perspective, the integration of OCT/OCTA and ERG with molecular pathology may provide a clinically feasible strategy for noninvasive monitoring of early retinal metabolic dysfunction before overt vascular lesions become detectable. Such an approach may be valuable for early disease screening, longitudinal monitoring, and therapeutic evaluation in diabetic retinal disease.

Several limitations should be considered when interpreting the present findings. First, the sample size was modest, and the correlation analyses should therefore be regarded as exploratory. Second, this study focused primarily on early-stage experimental DR, whereas the role and imaging correlates of ferroptosis in advanced or proliferative DR remain unclear. Third, molecular measurements were performed using bulk retinal tissue and therefore lacked cell-type specificity. Fourth, although Lx-1 treatment supports the potential involvement of ferroptosis-related pathways, its pleiotropic antioxidant effects cannot be completely excluded. Future studies integrating larger cohorts, cell-specific molecular assays, single-cell transcriptomics, spatial proteomics, or cell-specific imaging approaches will be important for identifying the retinal cell populations most susceptible to ferroptosis-associated injury.

5. Conclusion

In conclusion, longitudinal OCT and OCTA detected early structural and microvascular abnormalities in STZ-induced diabetic rats that co-occurred with retinal electrophysiological impairment and ferroptosis-associated metabolic alterations. Liproxstatin-1 partially preserved these imaging and functional phenotypes while attenuating molecular abnormalities. The data support OCT/OCTA-derived retinal thickness and vascular flow metrics as noninvasive phenotypic readouts of early diabetic retinal injury associated with ferroptosis-related stress, but not as ferroptosis-specific biomarkers. Larger and mechanistically targeted studies are warranted to determine the reproducibility, cellular origin, and translational value of these imaging-to-molecular associations.

Declarations

Author Contribution

Chuan Peng wrote the main manuscript text, Xiangning Wang provide information access，Jiabiao Liu and Mingjie Ni verify the information for accuracy，Wenjuan Wu and Shengxi Men statistical data，Cuixia Da make overall revisions to the article，All authors reviewed the manuscript.

Acknowledgements

This work is supported by the National Natural Science Foundation of China (62175156), the Science and Technology Innovation Project of the Shanghai Science and Technology Commission (22S31903000), the College-Level Project Fund of Shanghai Sixth People's Hospital (Grant No. ynlc201909), the Interdisciplinary Program of Shanghai Jiao Tong University (Project No. YG2022QN089), and Shanghai Sixth People's Hospital Project (ynnkxyb202415, SZB2025205, 20250107).

Disclosures.

The authors declare no conflicts of interest.

Data availability.

The data that support the findings of this study are available from the corresponding author upon reasonable request.

References

1. Yau JW, Rogers SL, Kawasaki R et al (2012) Global prevalence and major risk factors of diabetic retinopathy. Diabetes Care 35(3):556–564
2. Dixon SJ, Lemberg KM, Lamprecht MR et al (2012) Ferroptosis: an iron-dependent form of nonapoptotic cell death[J]. Cell 149(5):1060–1072
3. He W, Chang L, Li X et al (2023) Research progress on the mechanism of ferroptosis and its role in diabetic retinopathy[J]. Front Endocrinol 14:1155296
4. Ouyang J, Zhou L, Wang Q (2023) Spotlight on iron and ferroptosis: research progress in diabetic retinopathy[J]. Front Endocrinol 14:1234824
5. Liu Q, Liu CQ, Yi WZ et al (2024) Ferroptosis contributes to microvascular dysfunction in diabetic retinopathy[J]. Am J Pathol 194(6):1078–1089
6. Malaviya P, Kumar J, Kowluru RA (2024) Role of ferroptosis in mitochondrial damage in diabetic retinopathy[J]. Free Radic Biol Med 225:821–832
7. Wang B, Jin Y, Ouyang X et al (2024) Ferroptosis contributes to diabetes-induced visual pathway neuronal damage via iron accumulation and GPX4 inactivation[J]. Metab Brain Dis 39(7):1459–1468
8. Gao S, Gao S, Wang Y et al (2023) Inhibition of ferroptosis ameliorates photoreceptor degeneration in experimental diabetic mice[J]. Int J Mol Sci 24(23):16946
9. Li C, Cai QH (2024) Two ferroptosis-specific expressed genes NOX4 and PARP14 are considered as potential biomarkers for the diagnosis and treatment of diabetic retinopathy and atherosclerosis[J].

Diabetol Metab Syndr 16(1):61
10. Mu L, Wang D, Dong Z et al (2022) Abnormal Levels of Serum Ferroptosis-Related Biomarkers in Diabetic Retinopathy[J]. J Ophthalmol 2022(1):3353740
11. Huang D, Swanson EA, Lin CP et al (1991) Opt coherence tomography[J] Sci 254(5035):1178–1181
12. Athwal A, Balaratnasingam C, Yu DY et al (2020) Optimizing 3D retinal vasculature imaging in diabetic retinopathy using registration and averaging of OCT-A[J]. Biomedical Opt Express 12(1):553–570
13. Fu Q, Li Y (2023) Investigation of Changes in the Thickness and Blood Flow of Choroidal and Retinal in Lens-Induced Myopia in Mice[J]. Optom Ophthalmol Vis Sci, 25(9)
14. Qiang Yang DF, Chen (June 2012) Microbead-Induced Ocular Hypertensive Mouse Model for Screening and Testing of Aqueous Production Suppressants for Glaucoma, vol 53. Investigative Ophthalmology & Visual Science, p 7
15. Prencipe M, Perossini M (2020) The photopic negative response (PhNR): measurement approaches and utility in glaucoma. Int Ophthalmol 40:3565–3576
16. Dongmei Liu Y, Shen (2021) Overexpression of BMP4 protects retinal ganglion cells in a mouse model of experimental glaucoma. Exp Eye Res 210:108728
17. Shao J, Bai Z, Zhang L et al (2022) Ferrostatin-1 alleviates tissue and cell damage in diabetic retinopathy by improving the antioxidant capacity ofthe Xc–GPX4 system[J]. Cell Death Discovery 8(1):426
18. Gao S, Gao S, Wang Y et al (2023) Inhibition of ferroptosis ameliorates photoreceptor degeneration in experimental diabetic mice[J]. Int J Mol Sci 24(23):16946
19. Lee JY, Kim M, Oh SB et al (2022) Superoxide dismutase 3 prevents early stage diabetic retinopathy in streptozotocin-induced diabetic rat model[J]. PLoS ONE 17(1):e0262396
20. Jiang F, Zhou L, Zhang C et al (2023) Malondialdehyde levels in diabetic retinopathy patients: a systematic review and meta-analysis[J]. Chin Med J 136(11):1311–1321
21. Liu C, Sun W, Zhu T et al (2022) Glia maturation factor-β induces ferroptosis by impairing chaperone-mediated autophagic degradation of ACSL4 in early diabetic retinopathy[J]. Redox Biol 52:102292
22. You M, Li X, Chen Z et al (2024) Liproxstatin-1 suppresses lipid peroxidation and inflammation in retinal cells under hyperglycemic stress[J]. Chem Eng J 487:147930

Figures

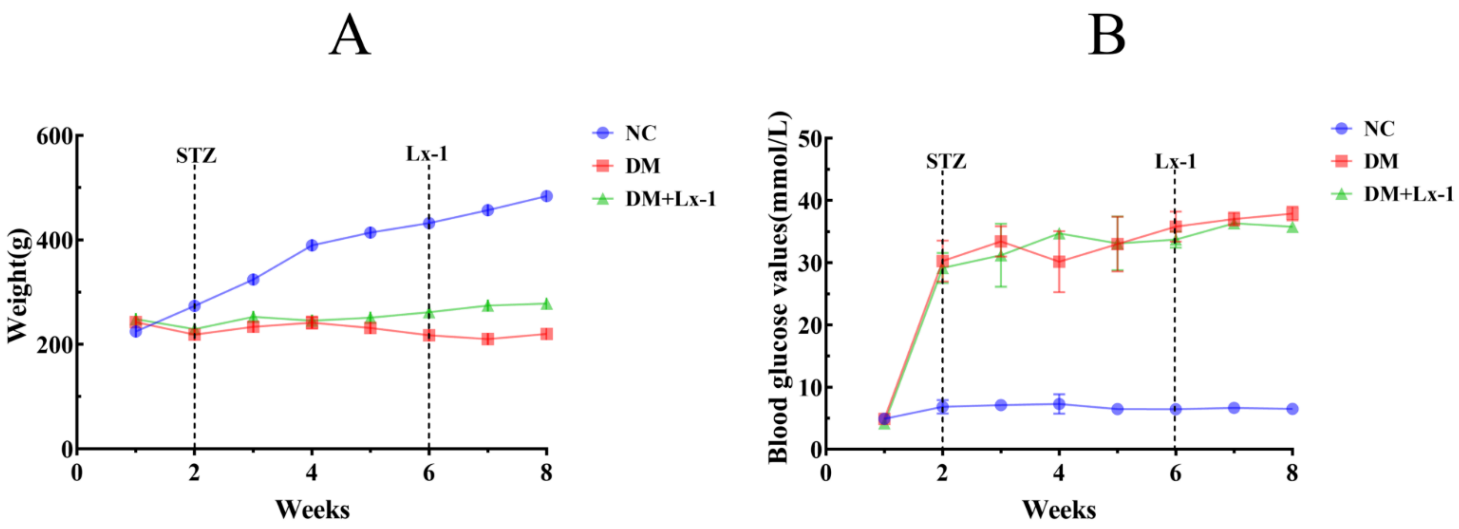


Figure 1

Changes in body weight and blood glucose levels of rats. (A-B) Quantitative analysis of body weight and blood glucose levels in each group. Data are presented as mean ± SD (n = 5). The dashed line labeled "STZ" marks the end of model induction, and "Lx-1" indicates the start of drug intervention.

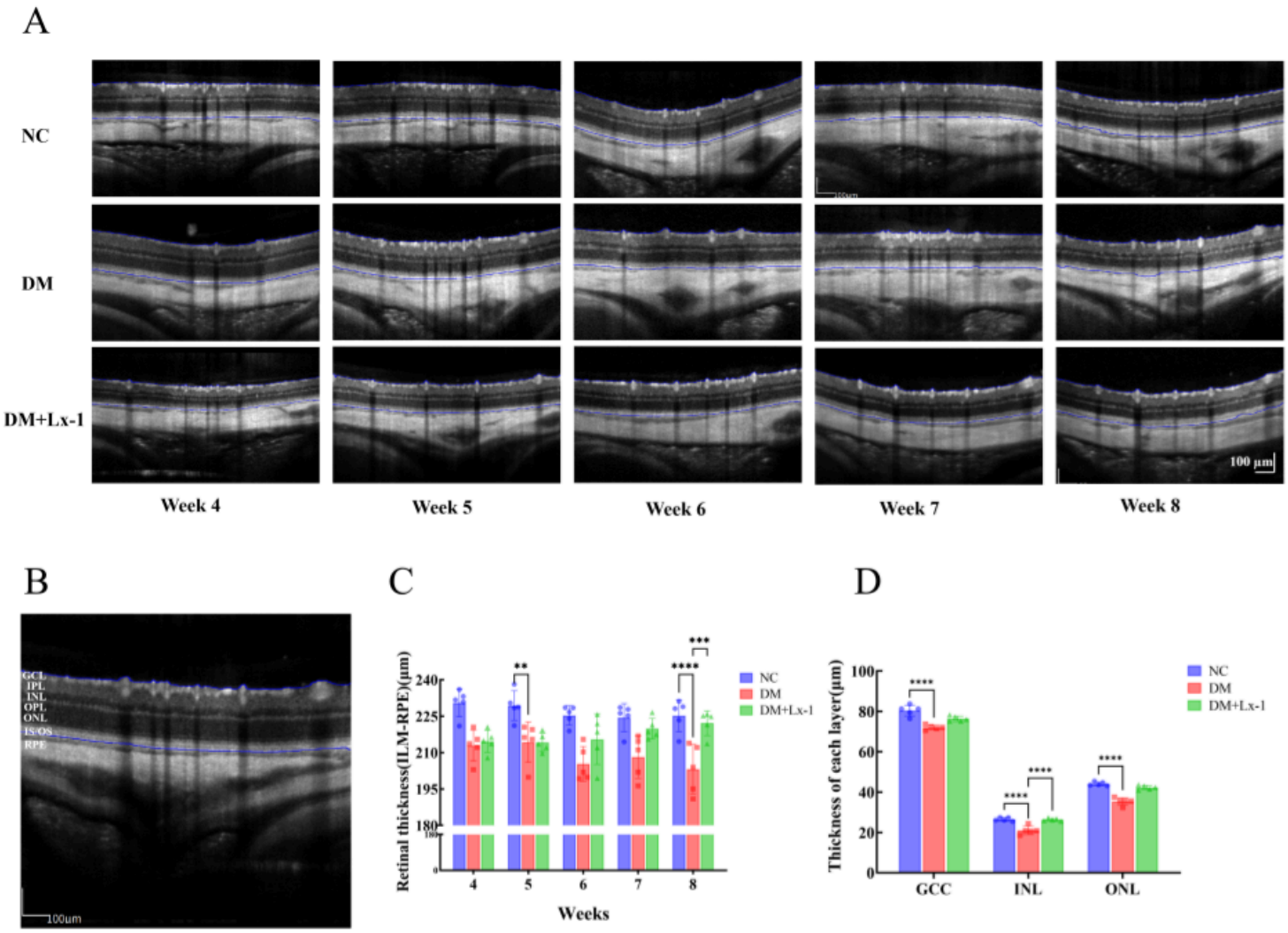


Figure 2

Longitudinal OCT images of the retina. (A) Representative retinal scans. Blue lines denote the internal limiting membrane (ILM) and RPE, which are used to define full retinal thickness. (B) Layered B-scan image of the retina. GCL, ganglion cell layer; IPL, inner plexiform layer; INL, inner nuclear layer; OPL, outer plexiform layer; ONL, outer nuclear layer; IS/OS, photoreceptor inner/outer segment junction; RPE, retinal pigment epithelium. (C-D) Quantitative analyses of full-thickness retinal thickness and selected sublayers (GCC, INL, ONL). Data are expressed as mean ± SD (n = 5). **p < 0.01, ***p < 0.001, ****p < 0.0001.

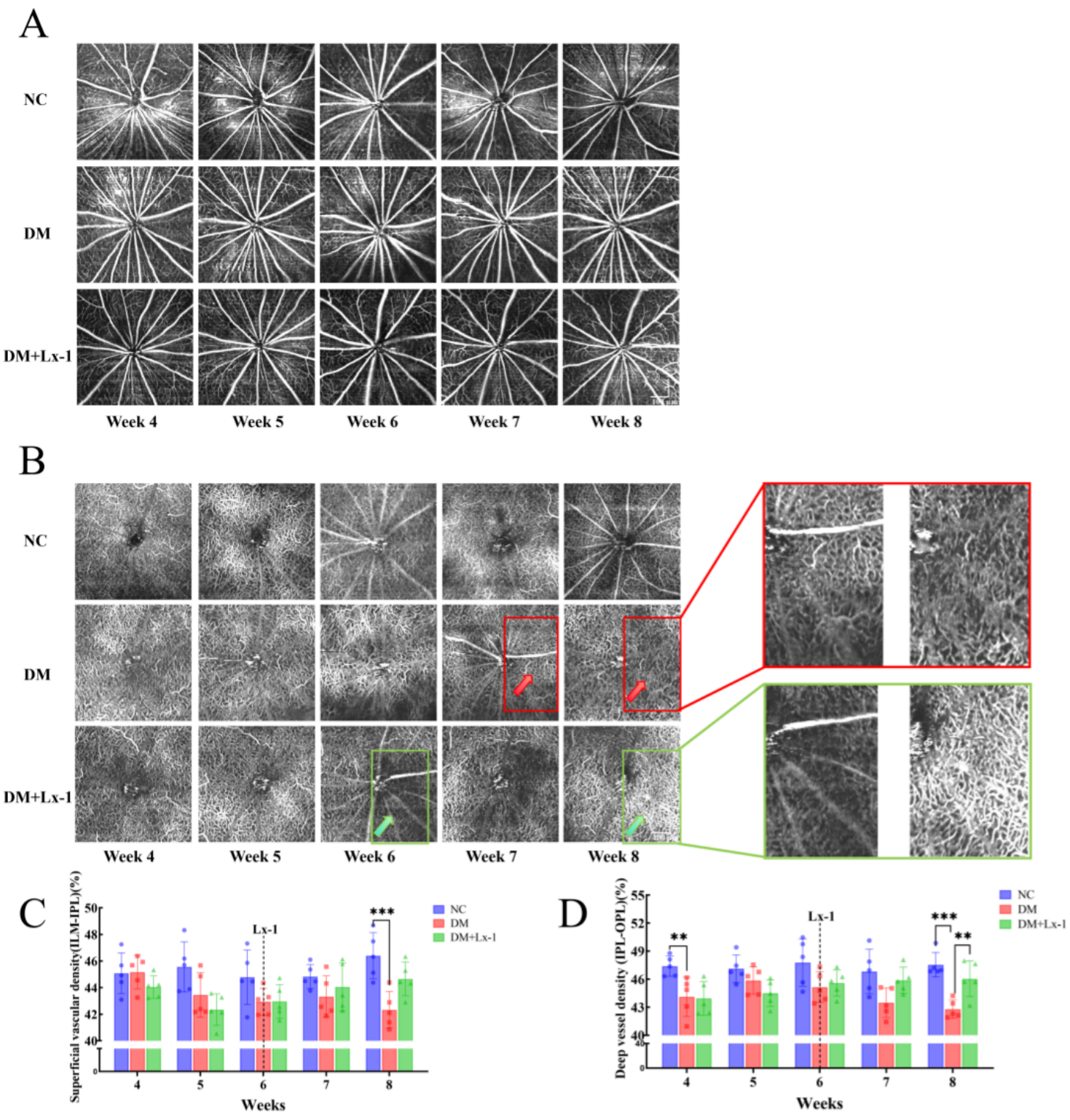


Figure 3

Changes in retinal vascular density. (A-B) Representative *en face* OCTA images, demonstrating changes in superficial and deep capillary plexus densities across the three experimental groups. Red and green markings indicate regions of capillary rarefaction and display magnified views of the areas denoted by the red and green arrows. (C-D) Temporal profiles of vascular density in the superficial and deep layers. Data are presented as mean ± SD. ***$p < 0.001$, **$p < 0.01$, *$p < 0.05$.

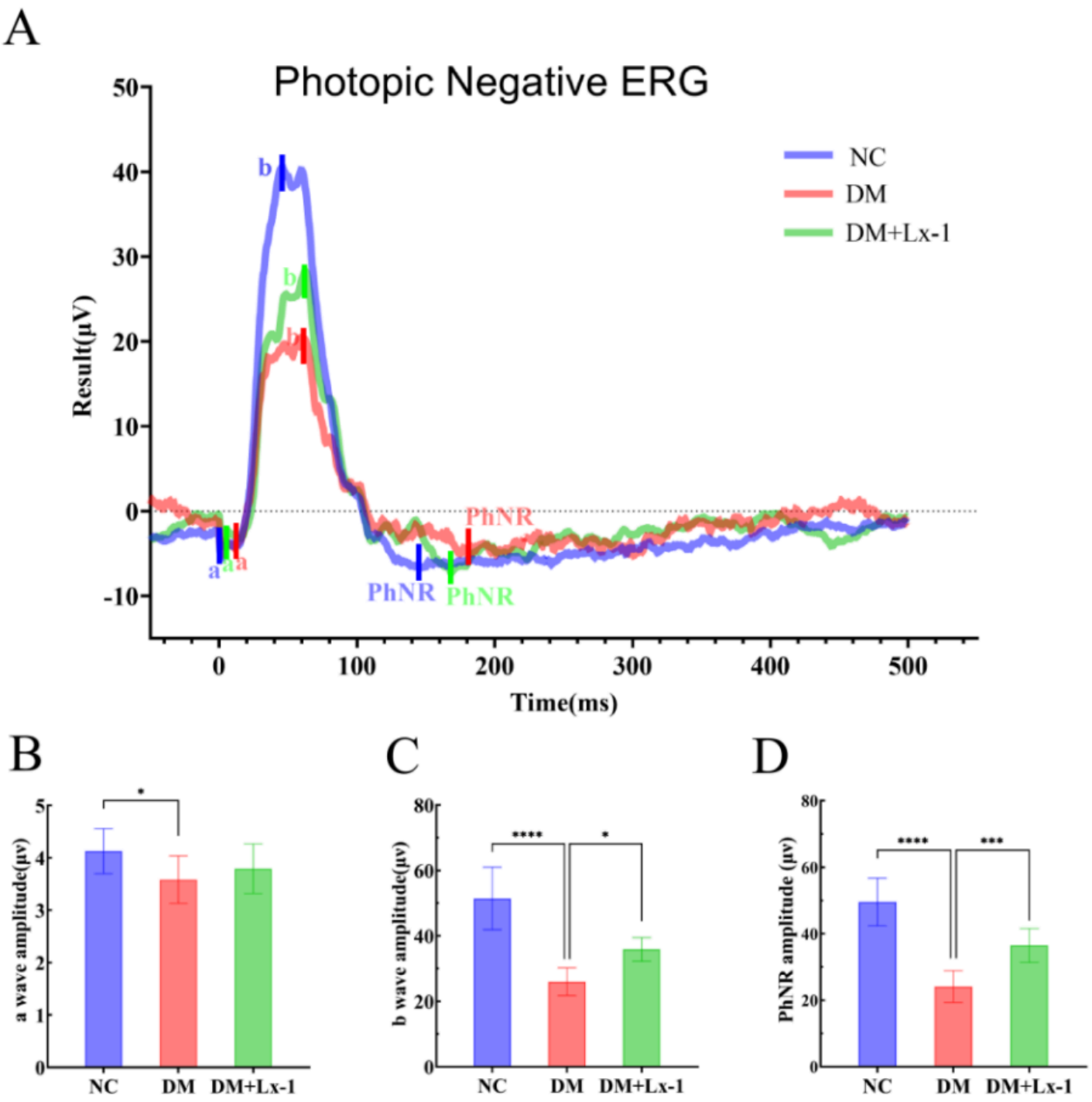


Figure 4

Alterations in retinal neural function under ferroptosis inhibition. (A) Photopic negative response (PhNR) electroretinograms recorded in each group. (B-D) Quantitative analysis of a-wave, b-wave, and PhNR amplitudes. Data are expressed as mean ± SD (n = 5). *p< 0.05,***p < 0.001, ****p< 0.0001.

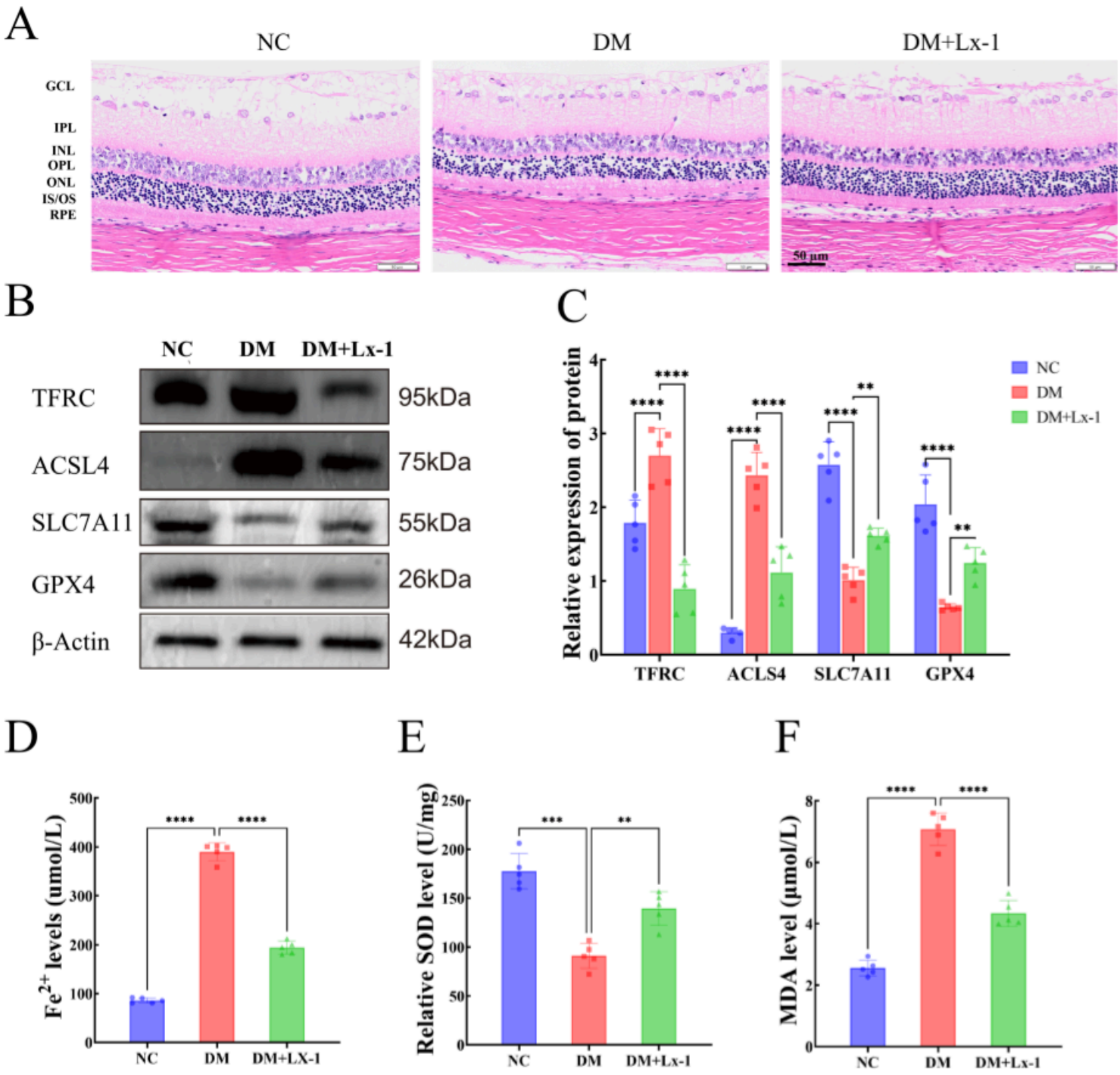


Figure 5

Retinal morphology and ferroptosis-associated measures. (A) Representative H&E-stained retinal sections. Scale bar: 50 μm. (B) Western blot analysis of TFRC, ACSL4, SLC7A11, GPX4, and β-actin. (C) Densitometric quantification normalized to β-actin. (D) Retinal Fe^{2+} concentration. (E) SOD activity. (F) MDA concentration. Data are mean ± SD (n = 5). **p < 0.01, ***p < 0.001, ****p < 0.0001 .

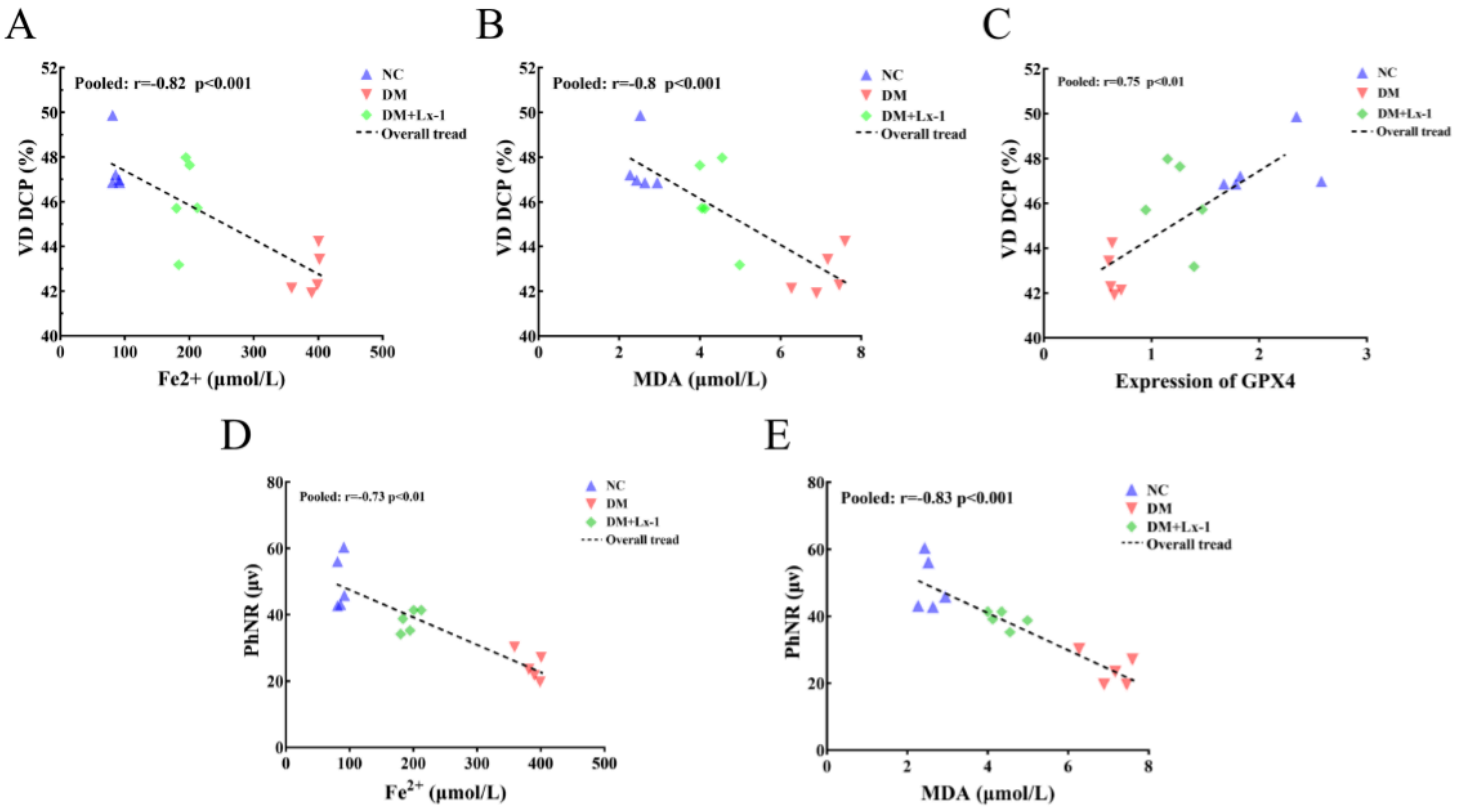


Figure 6

Exploratory associations between retinal phenotypes and ferroptosis-associated measures. (A-C) DCP vessel area density versus Fe^{2+} concentration, MDA concentration, and GPX4 expression, respectively. (D,E) PhNR amplitude versus Fe^{2+} and MDA, respectively. Each point represents one animal; colors indicate experimental groups. Dashed lines show pooled linear regression fits across all three groups.

Supplementary Files

This is a list of supplementary files associated with this preprint. Click to download.

- SupplementaryFigureS1.docx